APL Materials

Sputtering growth of $Y_3Fe_5O_{12}$/Pt bilayers and spin transfer at $Y_3Fe_5O_{12}$/Pt interfaces

Cite as: APL Mater. **5**, 126104 (2017); https://doi.org/10.1063/1.5013626
Submitted: 20 April 2017 • Accepted: 05 November 2017 • Published Online: 04 December 2017

Houchen Chang, Tao Liu, Danielle Reifsnyder Hickey, et al.

Sputtering growth of $Y_3Fe_5O_{12}$/Pt bilayers and spin transfer at $Y_3Fe_5O_{12}$/Pt interfaces

Houchen Chang,[1] Tao Liu,[1] Danielle Reifsnyder Hickey,[2] P. A. Praveen Janantha,[1] K. Andre Mkhoyan,[2] and Mingzhong Wu[1,a]
[1]*Department of Physics, Colorado State University, Fort Collins, Colorado 80523, USA*
[2]*Department of Chemical Engineering and Materials Science, University of Minnesota, Minneapolis, Minnesota 55455, USA*

(Received 20 April 2017; accepted 5 November 2017; published online 4 December 2017)

For the majority of previous work on $Y_3Fe_5O_{12}$ (YIG)/normal metal (NM) bi-layered structures, the YIG layers were grown on $Gd_3Ga_5O_{12}$ first and were then capped by an NM layer. This work demonstrates the sputtering growth of a Pt/YIG structure where the Pt layer was grown first and the YIG layer was then deposited on the top. The YIG layer shows well-oriented (111) texture, a surface roughness of 0.15 nm, and an effective Gilbert damping constant less than 4.7×10^{-4}, and the YIG/Pt interface allows for efficient spin transfers. This demonstration indicates the feasibility of fabricating high-quality NM/YIG/NM tri-layered structures for new physics studies.
https://doi.org/10.1063/1.5013626

Recently there is a strong interest in studying $Y_3Fe_5O_{12}$ (YIG)-based spintronics, and this interest is mainly driven by the fact that YIG materials have a damping constant lower than any other magnetic materials. In terms of the Gilbert model, the damping constant (α) in YIG materials is found to be $\alpha \approx 3 \times 10^{-5}$, which is two orders of magnitude lower than that in conventional ferromagnetic metals.[1] Apart from the low damping feature, YIG materials are also electrically insulating, shunting no current when an electric current flows in a neighboring normal metal (NM) or topological insulator (TI) layer.

The majority of the previous studies on YIG spintronics utilized YIG films that were grown on single-crystal $Gd_3Ga_5O_{12}$ (GGG) substrates first and then capped with either a thin NM layer[2–10] or a thin TI layer.[11–13] The use of the GGG substrates is crucial in terms of realizing high-quality YIG films because GGG not only has a crystalline structure almost perfectly matching that of YIG but is also extremely stable at high temperature in oxygen, which is the condition needed for YIG crystallization. The growth of the NM or TI capping layer on the top of YIG, on the other hand, is fairly easy to achieve and usually does not alter the properties of the YIG layer except enhancing the damping via spin pumping.

This letter reports on the feasibility of growing high-quality YIG thin films on Pt thin films. Generally speaking, it is technically challenging to grow high-quality YIG films on metallic films, and possible issues include the oxidation and peeling-off of the metallic layer, interfacial diffusion, and formation of pin-holes in the films during the growth or post-annealing process of the YIG films. In this work, a unique sputtering process was developed that successfully resolved these issues.

The feasibility demonstrated in this work is of great significance because it enables the fabrication of sandwich-like NM/YIG/NM or NM/YIG/TI structures. Such tri-layered structures will facilitate various interesting fundamental studies as well as device developments where, for example, one can use the top NM or TI layer as a writing layer to induce precession dynamics, domain wall motion, or even magnetization reversal in the middle YIG layer and use the bottom NM layer as a reading layer to probe the magnetization status in the YIG layer.

[a]Author to whom correspondence should be addressed: mwu@colostate.edu

In fact, in 2016, Pt/YIG/Pt sandwich structures have been used, independently by Wu *et al.*[14] and Li *et al.*,[15] to demonstrate for the first time magnon-mediated electric current drag, a phenomenon predicted by Zhang and Zhang in 2012.[16] However, in spite of the intriguing physics which those studies demonstrated, the YIG layers in the structures exhibited low quality. Specifically, in the work by Li *et al.*, the YIG layers had a low resistivity and underwent current leakage at room temperature (RT),[15] and in the work by Wu *et al.*, the YIG layers showed a large peak-to-peak ferromagnetic resonance (FMR) linewidth (ΔH), about 358 Oe at 9 GHz.[14]

Presented below is the use of an optimized sputtering process to grow YIG/Pt bi-layers on GGG substrates that show high quality in terms of the FMR linewidth, damping, resistivity in the top YIG layer, and spin transfer across the YIG/Pt interface. In a YIG(58 nm)/Pt(14 nm)/GGG(0.5 mm) structure, the YIG layer showed ΔH = 7.5-9.5 Oe over 8.5-17.5 GHz, which is considerably smaller than the ΔH value cited above,[14] and an effective damping constant less than 4.7×10^{-4}, which is comparable to the α value in YIG films grown on GGG substrates by pulsed laser deposition (PLD).[17–20] Efficient spin transfer across the YIG/Pt interface is indicated by strong inverse spin Hall voltage signals produced in the Pt layer by spin pumping.

Both the Pt and YIG layers were deposited by sputtering, and the deposition was on 0.5-mm-thick, (111)-oriented, single-crystal GGG substrates. There are three major procedures: (i) Pt deposition by DC sputtering, (ii) YIG deposition by RF sputtering at RT, and (iii) post-annealing at high temperatures. For the Pt deposition, the GGG substrate temperature plays a rather critical role. The Pt layers deposited at RT exhibit smooth surfaces but encompass large tensile stress,[21] and stress releasing during the later annealing process often produces bumps and spikes on the surface of the top YIG layer, as indicated in Fig. S4(b) of the supplementary material. On the other hand, deposition at temperatures higher than 300 °C can yield Pt films with much less tensile stress,[21] but such films are usually granular and exhibit very rough surfaces, as shown in Fig. S4(a) of the supplementary material, that affect the subsequent YIG deposition and prevent the realization of high-quality YIG/Pt interfaces. As a result, a two-step Pt growth process is taken. First, a 3-nm-thick Pt is deposited at 400 °C. Then a 11-nm-thick Pt is deposited at RT, showing a very smooth surface. The Pt growth is then followed by the deposition of an amorphous YIG layer by RT sputtering and then two distinct annealing steps. The first annealing is done at 650 °C for 60 min. The second annealing is carried out at 700 °C for 30 min. It is found that a one-step annealing process with various temperatures and time cannot guarantee a smooth and intact YIG layer, as indicated by Fig. S3 of the supplementary material. The two-step annealing process is to make sure that the YIG layer is crystallized, and at the same time, a smooth surface is maintained. For the data shown below, the sample was prepared using the optimized sputtering and annealing parameters listed in Table I of the supplementary material. The other parameters that are not listed are approximately the same as those described in Ref. 22.

Figures 1 and 2 give the representative data that show the structural and morphologic properties of an YIG(58 nm)/Pt(14 nm)/GGG(0.5 mm) sample fabricated with the parameters listed in Table I of the supplementary material. Figures 1(a) and 1(b) present two high-angle annular dark-field (HAADF) scanning transmission electron microscopy (STEM) images of the sample cross section using different scales, as indicated. The STEM measurements used an FEI Titan G2 60–300 S/TEM system equipped with a Schottky X-FEG gun and operated at 200 kV. Figures 1(c) and 1(d) show an atomic force microscopy (AFM) surface image and an X-ray diffraction (XRD) spectrum of the sample, respectively. The STEM images in Figs. 1(a) and 1(b) clearly indicate that the Pt layer manifests itself as a granular film with a smooth bottom surface and a rough top surface. The further analysis indicates that the Pt grains have an average lateral size of about 27 nm. The YIG layer is crystallized and exhibits (111) orientation, as shown in Figs. 1(b) and 1(d), and the top surface of the YIG layer is very smooth, as shown in Figs. 1(a) and 1(c). Several notes should be made. First, prior to the annealing, the YIG film is amorphous as it is deposited at RT and the FMR measurement shows no magnetic response. The above results indicate that during the annealing the YIG film is crystallized on the Pt layer though with large lattice mismatch. This is consistent with the previous work on Bi-doped YIG films, where amorphous films coated on glass substrates also become crystalline after the annealing.[23] Note that one cannot tell the crystalline texture of the Pt layer from the STEM images, indicating that the Pt layer may be nanocrystalline. As a result, the reason for the formation of the YIG (111) texture on the Pt layer is currently unknown. Second, the analysis of the AFM data

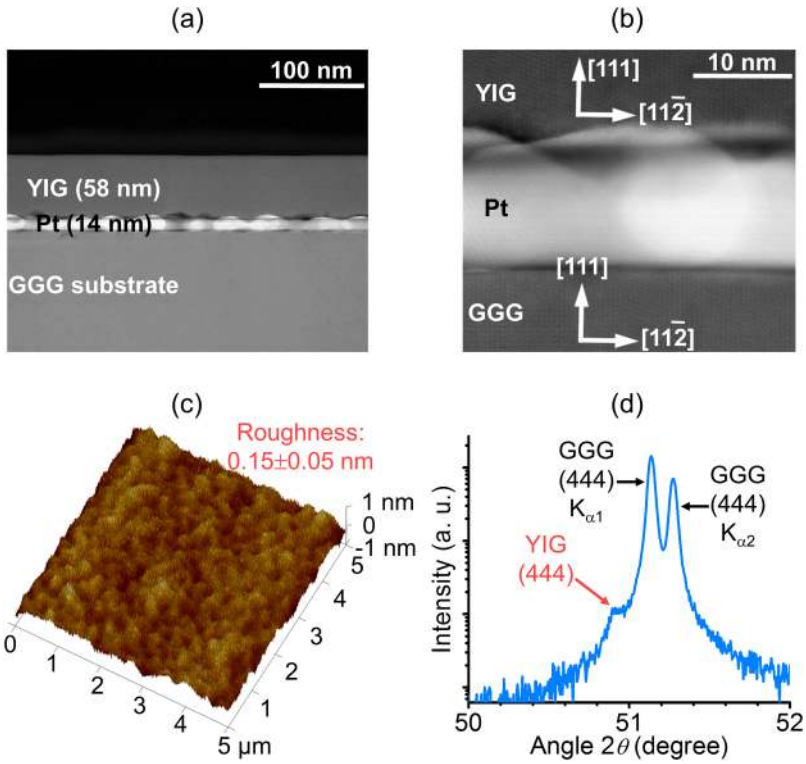

FIG. 1. Structural and morphologic properties of YIG(58 nm)/Pt(14 nm)/GGG(0.5 mm). (a) HAADF-STEM cross-sectional image. (b) HAADF-STEM cross-sectional image with a scale 10 times bigger than that in (a). (c) AFM surface image. (d) XRD spectrum.

indicates that the YIG film surface has a rms roughness of about 0.15 ± 0.05 nm. Third, the two-step Pt deposition process and the two annealing steps described above played important roles in the realization of the smooth YIG surface, and the latter is critical for achieving a high-quality interface if an additional NM or TI layer is grown on the top of the YIG layer. More discussions and control experiments about the Pt deposition and the annealing process are provided in the supplementary material.

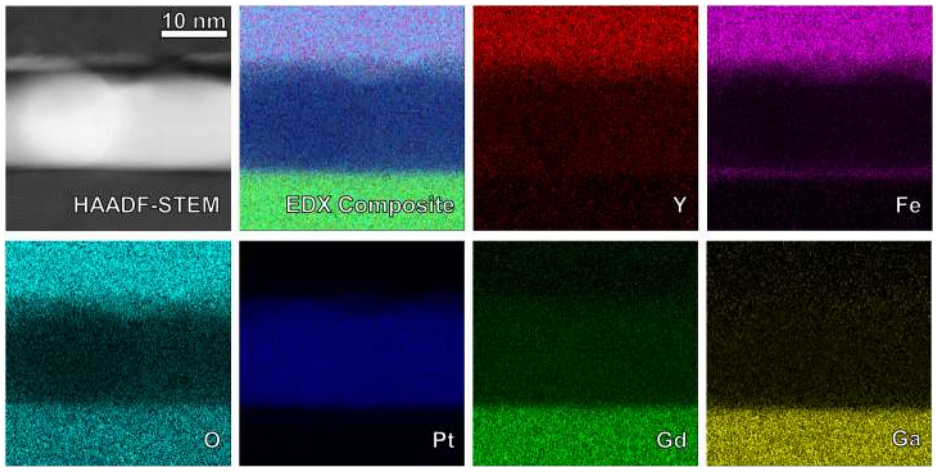

FIG. 2. HAADF-STEM image (top-left) and corresponding EDX compositional maps. The composite intensity (at. %) for individual-element maps has been rescaled for visibility.

Figure 2 presents the cross-sectional compositional maps measured with energy-dispersive X-ray (EDX) spectroscopy. Except the one for Fe, the EDX maps all indicate clear boundaries between the layers, suggesting very weak interfacial diffusion. In particular, the maps indicate that Pt, Ga, and Gd are all absent in the YIG layer. Surprisingly, Fe is clearly present at the GGG/Pt interface, possibly due to the diffusion of Fe from the YIG layer through the Pt layer during the annealing. It is fortunate that the presence of Fe at the GGG/Pt interface does not affect the spin transfer across the Pt/YIG interface and will therefore not play roles in the study of spin effects in Pt/YIG/NM or Pt/YIG/TI if such tri-layered structures are fabricated. In addition to the EDX maps, EDX line scans across the 5 nm depth of the YIG film were also obtained. The data, presented in Fig. S2 of the supplementary material, indicate an atomic Y/Fe ratio of 3/5, which is as expected. The EDX results together with the XRD results shown in Fig. 1(d) and Fig. S1 of the supplementary material confirm the composition of the YIG film and the absence of other oxide phases in the sample.

Figure 3 presents the magnetic hysteresis responses measured by a vibrating sample magnetometer (VSM) using different fields, as indicated. The analysis of the data in Fig. 3(a) yields a coercivity of $H_c \approx 20$ Oe and a saturation induction of $4\pi M_s \approx 1.37$ kG. The analysis of the data in Fig. 3(b) indicates $4\pi M_s \approx 1.58$ kG and a saturation field of about 1.52 kG. These values are compared with the corresponding values from the FMR and spin pumping measurements shortly.

Figure 4 presents the FMR data measured with shorted X-band and Ku-band waveguides. Figures 4(a) and 4(b) give the derivatives of the FMR power absorption for in-plane and out-of-plane fields, respectively. The circles show the data, while the red curves show the Lorentzian fits. The Lorentzian fitting-yielded FMR field (H_{FMR}) and ΔH data are presented in Figs. 4(c)–4(f).

In Figs. 4(c) and 4(d), the symbols show H_{FMR} as a function of frequency (f), while the lines show the fits to the Kittel equations

$$f = |\gamma| \sqrt{H\,(H + M_{eff})} \tag{1}$$

and

$$f = |\gamma|\,(H - 4\pi M_{eff}), \tag{2}$$

where $|\gamma|$ is the absolute gyromagnetic ratio, H is the external magnetic field, and M_{eff} is the effective saturation induction. Equations (1) and (2) are for the field-in-plane and field-out-of-plane configurations, respectively. The $|\gamma|$ and M_{eff} values indicated in Figs. 4(c) and 4(d) were obtained from the fitting. One can see that the two $|\gamma|$ values are very close to each other and they both are also close to the standard value (2.8 MHz/Oe).

In Figs. 4(e) and 4(f), the symbols show ΔH as a function of f, and the lines show fits to

$$\Delta H = \frac{2\alpha}{\sqrt{3}\,|\gamma|} f + \Delta H_0, \tag{3}$$

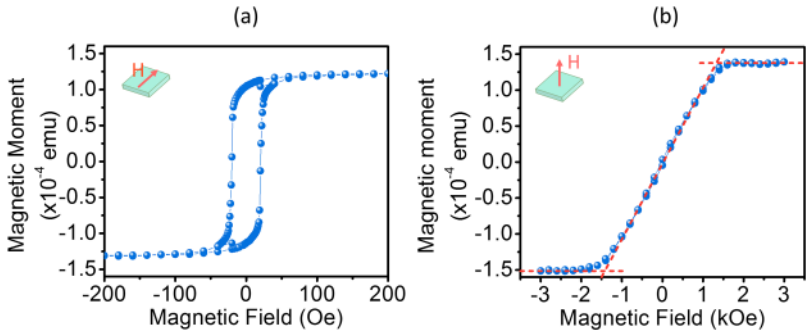

FIG. 3. Static magnetic properties: (a) and (b) show the hysteresis loops measured by a vibrating sample magnetometer using different fields, as indicated. The sample size is 5 mm × 4 mm. The dashed lines in (b) indicate how the saturation field is determined.

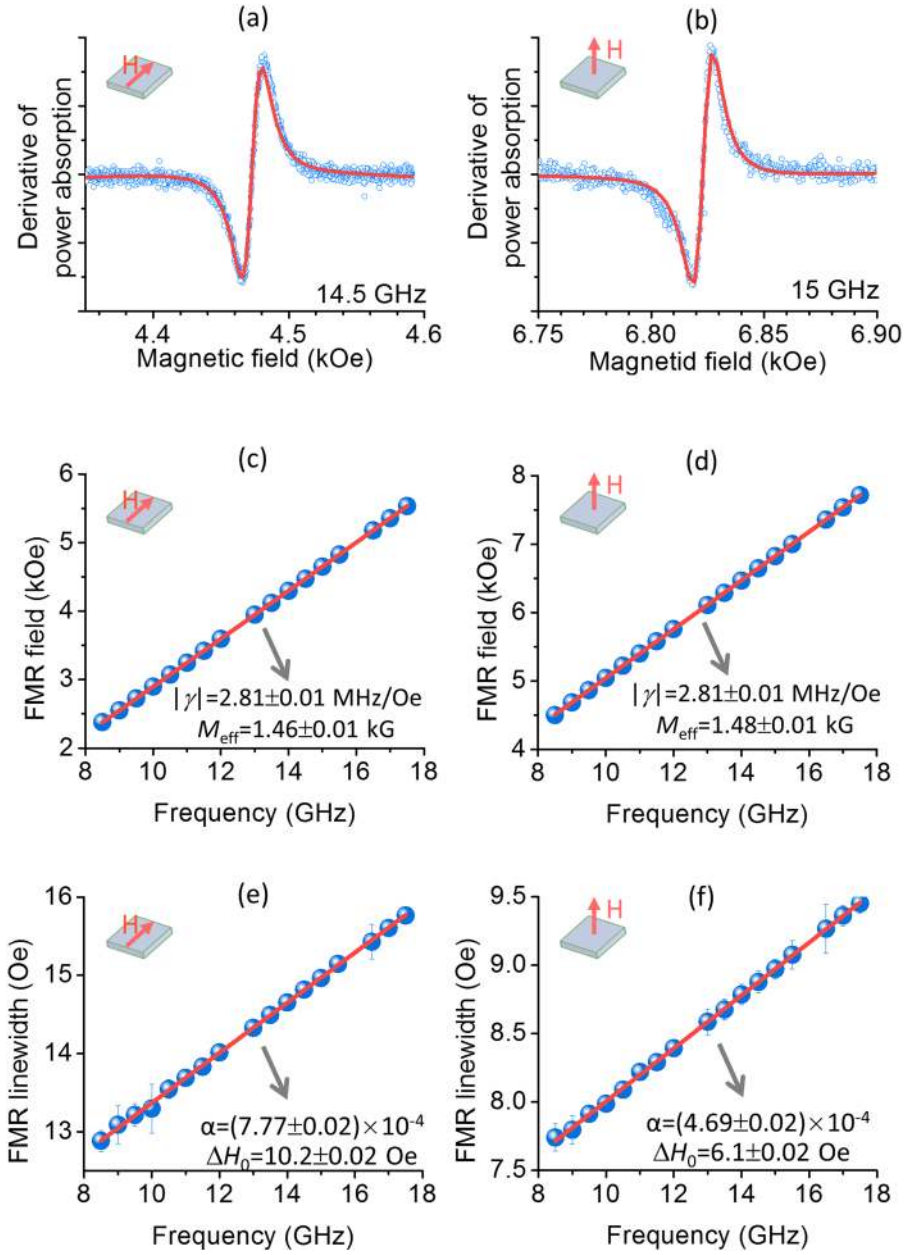

FIG. 4. FMR properties: (a) and (b) present the FMR profiles measured with in-plane and out-of-plane fields, respectively. The circles show the data, and the curves show the Lorentzian fits. (c) and (d) plot the Lorentzian fitting-yielded FMR field as a function of the frequency for two different field configurations, as indicated. (e) and (f) present the fitting-yielded FMR linewidth as a function of the frequency for different fields, as indicated. In (c)-(f), the symbols show the data, while the lines show the fits.

where α is the effective Gilbert damping constant, and ΔH_0 accounts for inhomogeneity linewidth broadening. The fitting-produced α and ΔH_0 values are also given in Figs. 4(e) and 4(f). The data indicate three important results. First, the linewidth values are slightly larger than those of the films grown on GGG substrates[17–20,22] but are substantially smaller than the value reported previously for the YIG films grown on Pt (about 358 Oe at 9 GHz).[14] Second, the ΔH vs. f response in Fig. 4(e) shows linear behavior over the entire frequency range, indicating that the two-magnon scattering is probably weak if it is present in the YIG film.[24,25] Third, the α value for the field-in-plane configuration is notably larger than that for the field-out-of-plane configuration. The same phenomenon also exists in

the Pt/YIG/GGG system as shown in Fig. S6 of the supplementary material. This difference is mainly from the difference in spin pumping for the two field configurations if one assumes the two-magnon scattering contribution is negligible. Previous theoretical work showed that in ferromagnet/non-magnetic metal bi-layers spin pumping-produced damping exhibits an anisotropic nature, being larger for in-plane fields than for out-of-plane fields.[26] Finally, considering that the damping constant of $(4.69 \pm 0.03) \times 10^{-4}$ given in Fig. 4(f) contains a contribution from spin pumping, one can conclude that the actual damping of the YIG film should be smaller than $(4.69 \pm 0.03) \times 10^{-4}$ and is therefore comparable to that of the YIG films grown on GGG substrates by PLD. The low α values reported previously for the PLD films include 2.3×10^{-4},[17,18] 2.2×10^{-4},[19] and 1.8×10^{-4}.[20]

The magnetic properties presented above clearly indicate that the YIG film grown on the Pt film exhibits high quality. They, however, do not speak for the quality of the YIG/Pt interface in terms of transfers of spins from one film to the other. To examine the interface quality, spin pumping experiments were carried out. During the measurements, one drives the magnetization precession in the YIG film by placing an end-shorted microstrip line on the top of the YIG film and feeding it with a microwave signal. The precession in the YIG layer pumps a pure spin current into the Pt layer that flows across the Pt thickness and produces an electrical voltage across the Pt lateral dimension via the inverse spin Hall effect (ISHE).[27]

Figure 5 presents the spin pumping data. Figure 5(a) sketches the experimental setup. Figure 5(b) presents a spin pumping signal map where the horizontal axis shows the strength of an external field applied along the $+x$ direction, the vertical axis shows the frequency of the microwave signal applied to the microstrip line, and the color shows the ISHE voltage (V_{ISHE}) measured across the Pt length (along the y axis). The blue dashed curve shows a fit to Eq. (1), and the fitting used $|\gamma| = 2.8$ MHz/Oe and took M_{eff} as the fitting parameter. Figure 5(c) shows the V_{ISHE} data measured in the same way as those shown in Fig. 5(b) except that the field was in an opposite direction (along the $-x$ direction). As the blue dashed curve in Fig. 5(b), the red dashed curve in Fig. 5(c) also shows a fit to Eq. (1). For both the measurements, the sample is 5.5 mm long and 2.5 mm wide, the microstrip line is 3.0 mm long and 50 μm wide and has a nominal impedance of 50 Ω, and the microwave power applied to the microstrip line is about 100 mW.

Several results are evident from the data in Fig. 5. First, the V_{ISHE} signals are strong, indicating that the interface allows for efficient spin transfers. The signal strength is close to those measured with Pt/YIG/GGG samples. For example, measurements using similar experimental configurations yielded V_{ISHE} = 10-50 μV for a Pt(8 nm)/YIG(20 nm)/GGG(0.5 mm) sample and $V_{\mathrm{ISHE}} \approx 24$ μV for a Pt(14 nm)/YIG(58 nm)/GGG(0.5 mm) sample. Second, the reverse of the field direction leads to a flip in the voltage sign. This is consistent with the fact that in spin pumping the direction of the magnetization in the magnetic layer dictates the polarization of the spin current pumped into the non-magnetic layer.[2,9] Third, the voltage signal is the strongest at about 2 GHz, and this is true for both the field directions. This is because the strength of the spin current in the Pt is proportional to $\sin^2\theta$, where θ is the angle of the magnetization precession in the YIG,[28] while for a given microwave power the precession angle in the YIG is frequency dependent and peaks at about 2 GHz if one takes a small-angle approximation. Detailed discussions about this frequency dependence are presented in the supplementary material. Lastly, the frequencies of the strongest voltage signals can be fitted

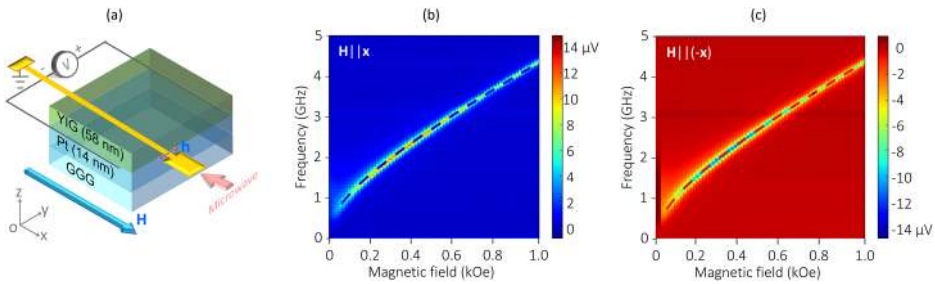

FIG. 5. Spin pumping measurements: (a) Experimental setup. (b) and (c) present the spin pumping-produced electrical voltage (color) measured across the Pt length as a function of the external field **H** (vertical axis) and the microwave frequency (vertical axis) for different field directions, as indicated. The dashed curves show the fits to Eq. (1).

nicely with Eq. (1), as shown by the dashed curves in Figs. 5(b) and 5(c), indicating that the spin pumping is mainly associated with the quasi-FMR modes in the portion of the YIG film right beneath the microstrip line. The fitting yields M_{eff} = 1.49 kG for the data in Fig. 5(b) and in Fig. 5(c). It should be noted that the linewidths of the spin pumping voltage signals are not comparable to the FMR linewidth values. This is because the microwave magnetic field produced by the microstrip line is spatially non-uniform and thereby excites non-uniform modes in the YIG film, as opposed to the spatially uniform microwave field and the uniform precession mode in the FMR experiments.

Finally, several points should be made about the quality of the YIG film. First, the above-mentioned six saturation induction values obtained from the VSM, FMR, and spin pumping measurements are all within 1.47 ± 0.10 kG, so they are reasonably close to each other. The small difference between those values may result from the VSM calibration error, the error in the YIG sample volume estimation, the slight misalignment of the fields in the FMR and spin pumping measurements, and the presence of weak crystalline anisotropy in the YIG film, among others. Second, the similarity of those values suggests that there is no notable anisotropy in the YIG film. Note that the crystalline anisotropy field in single-crystal YIG bulk materials is usually several tens of oersteds. Third, the average value 1.47 kG is about 16% lower than the well accepted bulk value (1.75 kG), and the reason for this big discrepancy is still unknown. The EDX analysis indicates that the YIG film has the right composition, but it is worth confirming this using more sensitive techniques. Fourth, the RT electrical resistance measurements on a 120-μm-long, 30-μm-wide Hall bar structure made of a Pt(3.0 nm)/YIG(58 nm)/Pt(14 nm)/GGG(0.5 mm) sample indicate that the YIG film has a resistivity higher than 1.4×10^9 Ω·m at RT, indicating the electrical insulating nature of the YIG film. For comparison, for the Pt/YIG/Pt structure reported in Ref. 15, the resistivity is significantly lower, about 9.6×10^5 Ω·m at 300 K and 1.9×10^7 Ω·m at 250 K. Finally, it is believed that it is possible to grow YIG thin films with similar quality on other metals rather than Pt as long as they have comparable or higher melting temperatures and have thermal expansion coefficients close to those of the substrate and YIG.

See supplementary material for the optimized sputtering process, detailed sample characterization by XRD, EDX, and AFM, discussions on the two-step Pt deposition process, spin pumping efficiency, frequency-dependent V_{ISHE} amplitude, electric contact of the sample, and Gilbert damping values in a Pt/YIG/GGG sample.

This work was primarily supported by SHINES, an Energy Frontier Research Center funded by the U.S. Department of Energy (No. SC0012670). The structure and interface characterizations were supported by C-SPIN. The spin pumping studies were supported by the U.S. National Science Foundation (No. EFMA-1641989). The STEM and EDX measurements utilized the College of Science and Engineering (CSE) Characterization Facility, University of Minnesota (UMN), supported in part by the NSF through the UMN MRSEC program (No. DMR-1420013); and the CSE Minnesota Nano Center, UMN, supported in part by NSF through the NNIN program.

[1] M. Sparks, *Ferromagnetic-Relaxation Theory* (McGraw-Hill, New York, 1964).
[2] Y. Kajiwara, K. Harii, S. Takahashi, J. Ohe, K. Uchida, M. Mizuguchi, H. Umezawa, H. Kawai, K. Ando, K. Takanashi, S. Maekawa, and E. Saitoh, Nature **464**, 262 (2010).
[3] G. L. da Silva, L. H. Vilela-Leão, S. M. Rezende, and A. Azevedo, J. Appl. Phys. **111**, 07C513 (2012).
[4] S. Y. Huang, X. Fan, D. Qu, Y. P. Chen, W. G. Wang, J. Wu, T. Y. Chen, J. Q. Xiao, and C. L. Chien, Phys. Rev. Lett. **109**, 107204 (2012).
[5] H. Nakayama, M. Althammer, Y.-T. Chen, K. Uchida, Y. Kajiwara, D. Kikuchi, T. Ohtani, S. Geprägs, M. Opel, S. Takahashi, R. Gross, G. E. W. Bauer, S. T. B. Goennenwein, and E. Saitoh, Phys. Rev. Lett. **110**, 206601 (2013).
[6] P. Pirro, T. Brächer, A. V. Chumak, B. Lägel, C. Dubs, O. Surzhenko, P. Görnert, B. Leven, and B. Hillebrands, Appl. Phys. Lett. **104**, 012402 (2014).
[7] J. Flipse, F. K. Dejene, D. Wagenaar, G. E. W. Bauer, J. Ben Youssef, and B. J. van Wees, Phys. Rev. Lett. **113**, 027601 (2014).
[8] M. Collet, X. de Milly, O. d'Allivy Kelly, V. V. Naletov, R. Bernard, P. Bortolotti, J. Ben Youssef, V. E. Demidov, S. O. Demokritov, J. L. Prieto, M. Muñoz, V. Cros, A. Anane, G. de Loubens, and O. Klein, Nat. Commun. **7**, 10377 (2016).
[9] M. B. Jungfleisch, W. Zhang, J. Sklenar, J. Ding, W. Jiang, H. Chang, F. Y. Fradin, J. E. Pearson, J. B. Ketterson, V. Novosad, M. Wu, and A. Hoffmann, Phys. Rev. Lett. **116**, 057601 (2016).
[10] K. Ganzhorn, S. Klingler, T. Wimmer, S. Geprägs, R. Gross, H. Huebl, and S. T. B. Goennenwein, Appl. Phys. Lett. **109**, 022405 (2016).
[11] Y. Fan, P. Upadhyaya, X. Kou, M. Lang, S. Takei, Z. Wang, J. Tang, L. He, L.-T. Chang, M. Montazeri, G. Yu, W. Jiang, T. Nie, R. N. Schwartz, Y. Tserkovnyak, and K. L. Wang, Nat. Mater. **13**, 699 (2014).

[12] Z. Jiang, C.-Z. Chang, M. R. Masir, C. Tang, Y. Xu, J. S. Moodera, A. H. MacDonald, and J. Shi, Nat. Commun. **7**, 11458 (2016).
[13] H. Wang, J. Kally, J. S. Lee, T. Liu, H. Chang, D. R. Hickey, K. A. Mkhoyan, M. Wu, A. Richardella, and N. Samarth, Phys. Rev. Lett. **117**, 076601 (2016).
[14] H. Wu, C. H. Wan, X. Zhang, Z. H. Yuan, Q. T. Zhang, J. Y. Qin, H. X. Wei, X. F. Han, and S. Zhang, Phys. Rev. B **93**, 060403 (2016).
[15] J. Li, Y. Xu, M. Aldosary, C. Tang, Z. Lin, S. Zhang, R. Lake, and J. Shi, Nat. Commun. **7**, 10858 (2016).
[16] S. S.-L. Zhang and S. Zhang, Phys. Rev. Lett. **109**, 096603 (2012).
[17] Y. Sun, Y. Y. Song, H. Chang, M. Kabatek, M. Jantz, W. Schneider, M. Wu, H. Schultheiss, and A. Hoffmann, Appl. Phys. Lett. **101**, 152405 (2012).
[18] O. d'Allivy Kelly, A. Anane, R. Bernard, J. B. Youssef, C. Hahn, A. H. Molpeceres, C. Carrétéro, E. Jacquet, C. Deranlot, P. Bortolotti, R. Lebourgeois, J.-C. Mage, G. de Loubens, O. Klein, V. Cros, and A. Fert, Appl. Phys. Lett. **103**, 082408 (2013).
[19] M. C. Onbasli, A. Kehlberger, D. H. Kim, G. Jakob, M. Kläui, A. V. Chumak, B. Hillebrands, and C. A. Ross, APL Mater. **2**, 106102 (2014).
[20] B. M. Howe, S. Emori, H.-M. Jeon, T. M. Oxholm, J. G. Jones, K. Mahalingam, Y. Zhuang, N. X. Sun, and G. J. Brown, IEEE Magn. Lett. **6**, 3500504 (2015).
[21] R. E. Rottmayer and R. W. Hoffman, J. Vac. Sci. Technol. **8**, 151 (1971).
[22] H. Chang, P. Li, W. Zhang, T. Liu, A. Hoffmann, L. Deng, and M. Wu, IEEE Magn. Lett. **5**, 6700104 (2014).
[23] A. Kirihara, K. Uchida, Y. Kajiwara, M. Ishiba, Y. Nakamura, T. Manako, E. Saitoh, and S. Yorozu, Nat. Mater. **11**, 686–689 (2012).
[24] R. D. McMichael and P. Krivosik, IEEE Trans. Magn. **40**, 2 (2004).
[25] K. Lenz, H. Wende, W. Huch, K. Baberschke, K. Nagy, and A. Janossy, Phys. Rev. B **73**, 144424 (2006).
[26] K. Chen and S. Zhang, Phys. Rev. Lett. **114**, 126602 (2015).
[27] A. Hoffmann, IEEE Trans. Magn. **49**, 5172 (2013).
[28] O. Mosendz, V. Vlaminck, J. E. Pearson, F. Y. Fradin, G. E. W. Bauer, S. D. Bader, and A. Hoffmann, Phys. Rev. B **82**, 214403 (2010).